11

Integration of InSAR and GNSS

11.1 Complementary Attributes of InSAR and GNSS

Interferometric synthetic aperture radar (InSAR) and the global navigation satellite system (GNSS) can provide measurements of surface deformation at the accuracy of 10 mm or better, yet they have very different spatial and temporal resolution. Continuously operating GNSS sites provide three components of surface deformation with 5–30 mm accuracy at high temporal sampling (1–15 seconds). As discussed in Chapter 9, the two frequencies of GNSS systems enable very accurate correction of the path delays through the ionosphere. In addition, tropospheric delays can be estimated and corrected by measuring the LOS path delay to numerous satellites as they transit across the sky. These multiple paths, combined with the high sampling rate and the assumption that the site is moving slowly relative to a 10-minute satellite transit, provide the atmospheric delay data needed to make a very accurate ionospheric and tropospheric noise correction. The main limitation of GNSS is the sparse spatial sampling. In densely instrumented regions such as Japan or California, the typical spacing of GNSS sites is 20 km or closer. However, in many remote areas, the site spacing may be 200 km or more. Because InSAR measures relative deformation with respect to a reference point, GNSS surface deformation observations are often used to calibrate InSAR measurements to the absolute reference frame of the Earth (including moving plates) as defined by the International Terrestrial Reference Frame ITRF20 (Altamimi et al., 2023).

InSAR has very different attributes. First, a single interferogram provides only one component of deformation in the LOS direction. Current InSAR-capable satellites do not have sufficient bandwidth to enable reliable ionospheric correction, so the longer-wavelength SAR systems (-L- and S-band) may have meter or more errors across the swath of an interferogram, especially in high-latitude regions. In addition, there is no spatial or temporal redundancy in a single interferogram, so it is not possible to correct for the tropospheric delay directly from InSAR data, which

is typically ~50–80 mm on larger scales (>100 km) and ~8 mm on scales less than 10 km (Figure 9.5). The temporal sampling of InSAR is much worse than GNSS. For example, the Sentinel-1 satellite(s) currently have a 12-day cadence, although when both S-1a and S-1b were operating, the cadence was 6 days in some locations. The COSMO-SkyMed system can achieve a 4-day revisit cycle, but these data are not freely available. While InSAR decorrelation commonly restricts the time span of individual interferograms to be less than a few months over vegetated regions due to temporal decorrelation, it is possible to use the SBAS method discussed in Chapter 10 to create longer time series. However, this limits the number of InSAR phase observations suitable as input for the SBAS inversion and reduces the ability to mitigate random tropospheric turbulence noise. Increasing the InSAR timespan using SBAS introduces large temporal errors on long timescales due to the noise and decorrelation in the individual interferogram unless external constraints are available.

The conclusion is that InSAR and GNSS measurement systems need to be combined to achieve high accuracy (<20 mm), high spatial resolution (<1 km), vector displacements, and long-timespan accuracy at a cadence of the InSAR system. A diagram crudely showing the space-time scales at which each system excels is shown in Figure 11.1. Note there is a small overlap zone, centered at the characteristic spacing of the GNSS sites and the time over which several interferograms can be combined to reduce the ionospheric/atmospheric noise. In this overlap zone, measurements from the two systems can be combined to achieve a single geodetic system with improved space/time sampling. However, such a combination for a single InSAR look direction time series still does not provide vector displacements. In this chapter we discuss the strengths and limitations of the InSAR systems, the methods of using GNSS data to improve the InSAR accuracy and temporal resolution, and ways to use multiple InSAR look directions and ancillary products such as pixel tracking and burst overlap interferometry to reconstruct vector deformation time series. There are many ways to approach this integration, so we will move from the simplest to the most advanced.

11.2 Vector Decomposition

As discussed in Chapter 7, the unwrapped phase of a single interferogram can be converted to a line-of-sight (LOS) deformation d_{los} map by multiplying by the λ and dividing by 4π

$$d_{los} = -\phi \frac{\lambda}{4\pi}. \tag{11.1}$$

where the extra factor of 2 is needed to account for the two-way travel time of the radar pulse. The negative sign is used to convert the range increase to a decrease in

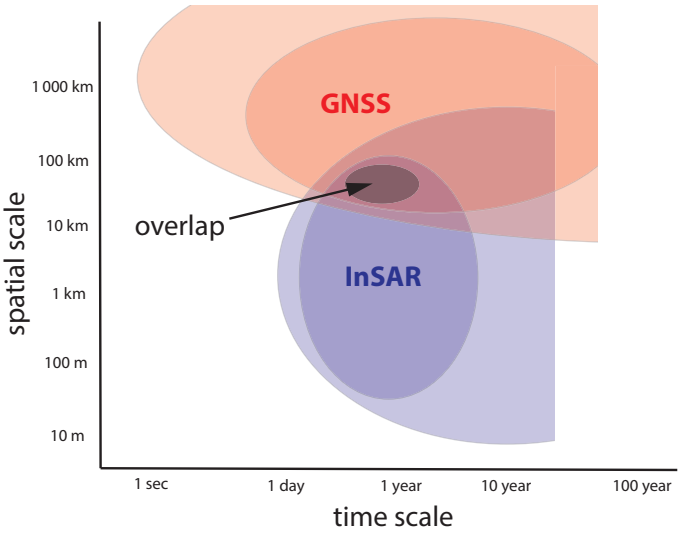

Figure 11.1 Schematic diagram showing the approximate spatial and temporal sampling of GNSS and InSAR systems; darker is better. GNSS has the highest accuracy and best range of temporal resolution from 1 second to the time span since numerous sites were installed ~30 years ago. InSAR has superior spatial resolution and broad spatial coverage, but the temporal resolution is limited by the cadence of the measurements. There is an overlap zone with a spatial scale of ~30–100 km and a time scale of one month to several years where the more accurate GNSS data can be used to bring the less accurate InSAR data into the global reference system (e.g., ITRF20, (Altamimi et al., 2023)).

the LOS distance between the ground and the spacecraft. Throughout this chapter we will use a local coordinate system of East, North, and Up (ENU) to match the coordinates commonly used by the GNSS and modeling communities.

As a first step, we use the location and elevation of a point on the ground to compute the look vector between that point and the satellite. For a particular point in the interferogram (lon, lat, elevation), we compute its Earth-centered Earth-fixed (ECEF) Cartesian coordinate (x_o, y_o, z_o) as shown in Figure 3.8 using Equation 3.13. Given the precise orbit, we can use the back project algorithm, described in Section 3.7.2, to calculate the position of the satellite at minimum range (x_s, y_s, z_s). The unit look vector $\mathbf{n}$ from the ground to the satellite is

$$\mathbf{n} = \frac{\mathbf{x}_s - \mathbf{x}_o}{|\mathbf{x}_s - \mathbf{x}_o|}. \tag{11.2}$$

Now we need to rotate this unit vector from the ECEF coordinates to the ENU coordinates. This involves two rotation matrices described at https://gssc.esa.int/navipedia/index.php/Transformations_between_ECEF_and_ENU_coordinates. First consider a simple case of the ENU axes located at 0° latitude and 0°

longitude. The E and N components are tangent to the ellipse of the Earth. The E axis is rotated 90° with respect to the Earth's x-axis and the U axis is rotated by –90° with respect to the Earth's z-axis. For proper alignment of an ENU frame at any latitude and longitude location, we need the following

$$\theta_r = \frac{\pi}{2} - \theta_g \tag{11.3}$$

$$\lambda_r = \frac{\pi}{2} + \lambda_g \tag{11.4}$$

where θ_g and λ_g are the geographic latitude (also called geodetic latitude) and longitude, respectively. Then two rotations are needed to transform a unit vector from the ECEF coordinates to the ENU coordinates

$$\mathbf{n}_{ENU} = \mathbf{R}_1\,(\theta_r)\,\mathbf{R}_3\,(\lambda_r)\,\mathbf{n} \tag{11.5}$$

where the two rotation matrices are given by

$$\mathbf{R}_1\,(\theta_r) = \begin{pmatrix} 1 & 0 & 0 \\ 0 & \cos\theta_r & \sin\theta_r \\ 0 & -\sin\theta_r & \cos\theta_r \end{pmatrix} \tag{11.6}$$

$$\mathbf{R}_3\,(\lambda_r) = \begin{pmatrix} \cos\lambda_r & \sin\lambda_r & 0 \\ -\sin\lambda_r & \cos\lambda_r & 0 \\ 0 & 0 & 1 \end{pmatrix} \tag{11.7}$$

There is a function in the GMTSAR software package called *SAT_look* that uses the precise orbit of the reference SAR image to compute a unit look vector $\mathbf{n}_{ENU}$ from the ground to the satellite at a particular geographic longitude, latitude, and elevation above the WGS84 ellipsoid.

Now we can transform a surface deformation vector, either from GNSS measurements $\mathbf{d}_{gnss}$ or a model output, to the LOS direction of an interferogram

$$d_{los} = \mathbf{d}_{gnss} \bullet \mathbf{n}_{ENU}. \tag{11.8}$$

Many studies assume this transformation is uniform over the entire frame of an interferogram. That is approximately true for the 100 km by 100 km frames of the European Remote Sensing satellite (ERS) and Envisat data. However, the incidence angle for Sentinel-1 varies from 29° in the near range to 46° in the far range, so we will consider that the unit look vector changes with position. One could compute the local incidence angle θ_i as

$$\theta_i = \tan^{-1}\frac{u}{\left(e^2 + n^2\right)^{1/2}} \tag{11.9}$$

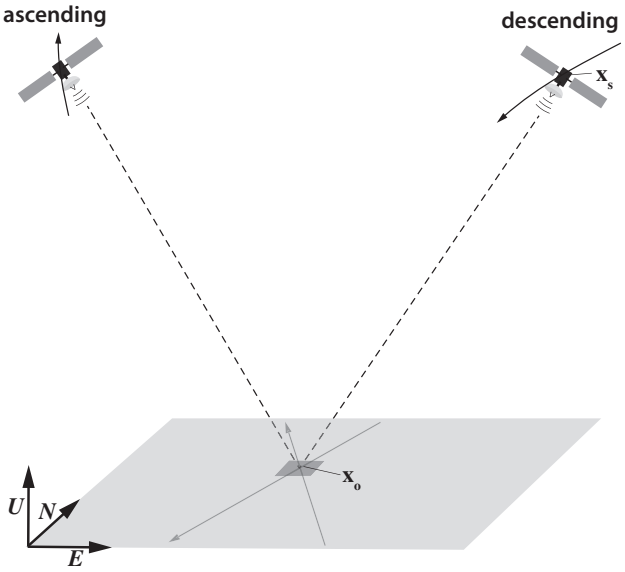

Figure 11.2 Schematic view of line of sight (LOS) measurements on ascending and descending satellite passes (after Fuhrmann and Garthwaite (2019)).

where $\mathbf{n}_{enu} = (e, n, u)$ are the components of the local ENU look vector. Similarly, the satellite azimuth is

$$\alpha = \tan^{-1} \frac{n}{e} \tag{11.10}$$

As discussed earlier, most InSAR satellites can provide surface deformation measurements along two look directions. When the deformations are large, pixel tracking methods, as discussed in Chapter 10, can provide a third component of deformation (Fialko et al., 2001).

Figure 11.2 shows the radar imaging geometry from ascending and descending look angles. First consider a pixel located exactly halfway between the two satellite tracks. In this case the look angle on the ascending and descending passes is equal. Also, the satellite azimuth of the two passes is equal but opposite in sign. For this ideal case, one can project the ENU deformation into the two LOS deformations measured by the satellite as

$$\begin{pmatrix} d_a \\ d_d \end{pmatrix} = \begin{pmatrix} e & n & u \\ -e & n & u \end{pmatrix} \begin{pmatrix} d_e \\ d_n \\ d_u \end{pmatrix}. \tag{11.11}$$

By subtracting the ascending and descending LOS deformations, one can uniquely relate the east motion to the difference between the two LOS measurements

$$d_a - d_d = 2ed_e. \tag{11.12}$$

The sum of the two LOS deformations gives

$$d_a + d_d = 2nd_n + 2ud_u. \tag{11.13}$$

Note the sum of the ascending and descending interferograms is a mixture of north and up displacement. For a typical mid-latitude ERS image, the ascending unit vector is (0.387 0.082 0.918). Here the unit vector for the north component is more than 10 times smaller than the up component and 4.7 times smaller than the east component. This is because at mid and low latitudes, the satellite track is only 13° from an N-S direction and the LOS measurement is almost perpendicular to the N-S vector. Since most InSAR satellites have high-inclination orbits, they are not sensitive to N-S deformation. Indeed, if one is studying a process that is dominated by vertical motions such as a hydrologic basin or volcanic inflation, one could ignore the N-S contribution to Equation 11.13 and relate the vertical deformation as $d_u = (d_a + d_d)\ /2u$. Moreover, if only the ascending or descending track is available, one may approximate the vertical deformation as $d_u = d_a/u$, although Fuhrmann and Garthwaite (2019) note that this latter approximation is not accurate for a finite size deformation feature with non-negligible east/west motions.

This simplified geometric analysis highlights the strengths and weaknesses of measuring deformation with InSAR. For example, InSAR is suitable for monitoring strike-slip deformation on an E-W-trending fault such as the North Anatolian fault in Turkey, but not suitable for monitoring strike-slip deformation on the N-S trending Dead Sea Transform. In a general case, we can compute the ENU look vectors for ascending and descending geometries at a pixel location and then perform the LOS decomposition similar to Equation 11.11.

11.3 Corrected GNSS LOS Displacement for Events

First consider a displacement event that occurs on a timescale shorter than the repeat cycles of an InSAR satellite. A good example is the 2019 Ridgecrest earthquakes. For this discussion, we consider the two earthquakes (M6.4 July 4 and M7.1 July 6) as a single event and ignore the postseismic deformation on the 12-day repeat timescale of Sentinel-1. The objective is to combine the InSAR and GNSS data to obtain the best possible surface displacement model.

A descending LOS displacement map, spanning both Ridgecrest, is shown in Figure 11.3 along with the positions of continuous GNSS sites. The large-scale errors were corrected using the GNSS sites in the area. The GMTSAR routine *SAT_look* uses the longitude, latitude, and elevation of each GNSS site, along with the orbital state vector for the SAR image, to create a different unit vector $\mathbf{n}_{ENU}$ for each GNSS site. The dot product of the unit vector and the vector displacement of the GNSS between the two times of the reference and repeat images results in

an estimate of the InSAR error at each site. These point errors are fit with a surface using a polynomial or 2-D spline that is subtracted from the interferogram to make the correction. A plot of the corrected LOS displacement and the GNSS LOS displacement is shown in Figure 11.3.

We note that there are many papers on this topic and many go far beyond this simple exercise to use ascending and descending passes from multiple satellites (e.g., Jin and Fialko (2020)) and pixel offsets from optical imagery to recover the near-fault horizontal displacements as well as GNSS time series and seismic waveforms to decompose the deformation from the M6.4 and 7.1 events (Antoine et al., 2021; Guns et al., 2022). Indeed, in most of these studies the ultimate objective is to invert for the slip at depth using all surface displacements available (e.g., Jin and Fialko (2020)).

11.4 Interseismic Velocity and Strain Rate

Unlike earthquake deformation, which typically ranges between 10s of cm and a few meters in a matter of seconds or minutes, interseismic velocities are slow and steady. Typical interseismic slip rates on active faults can range from <1 mm/yr (e.g., the Longmenshan Fault (Zhang, 2013)) to >30 mm/yr (e.g., the San Andreas Fault (Guns et al., 2022)). Such rates can be easily dwarfed by noise in a single interferogram (e.g., tens of millimeters). Therefore, long time series (Chapter 10) derived from hundreds of high-quality interferograms (with major noise terms corrected; see Chapter 9) are typically required to constrain interseismic velocity to an accuracy of 1 mm/yr. This velocity accuracy gives an equivalent strain rate accuracy of 100 nanostrain/yr over 10 kilometers, a distance comparable to typical fault locking depth, thus useful for seismic hazard assessment (Xu et al., 2021).

We can calculate the theoretical uncertainty of interseismic LOS velocity, σ_v, using

$$\sigma_v \simeq \frac{2\sqrt{3}\sigma_e}{\sqrt{N}T} \tag{11.14}$$

where σ_e is the time series uncertainty per epoch, N is the total number of epochs, and T is the total time span of the time series in years (Zhang et al., 1997). The epoch uncertainty is a function of the coherence of interferograms and the quality of atmospheric and earth tide corrections. Using $\sigma_e \approx 10$ mm as a rough estimate for C-band time series after tropospheric correction (Morishita et al., 2020), a 1 mm/yr velocity uncertainty requires at least 60 epochs over 4.5 years (Ou et al., 2022).

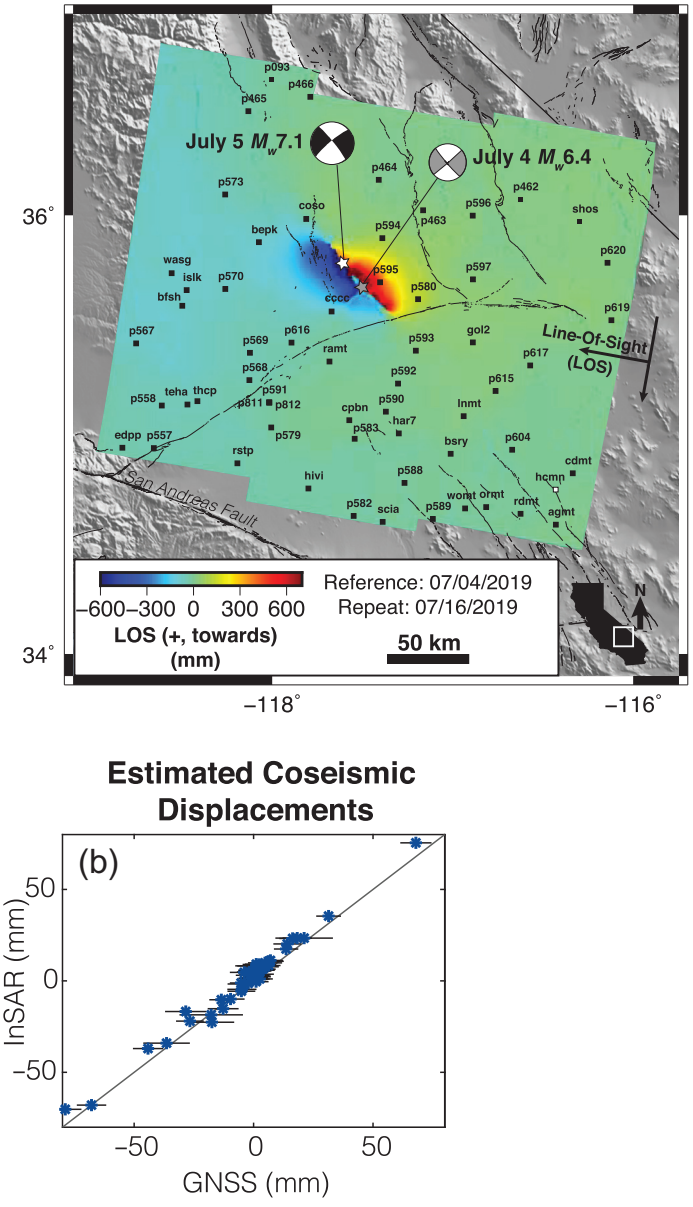

Figure 11.3 (a) Descending LOS unwrapped interferogram spanning the two Ridgecrest earthquakes. Continuously operating GNSS stations within the frame of the interferogram were used to correct long-wavelength errors due to atmospheric, ionospheric, and orbital errors. (b) After correction, the RME misfit between the GNSS and InSAR data is 13 mm (Guns et al., 2022).

The horizontal strain rate tensor, $\dot{\varepsilon}_h$, is the symmetrical part of the horizontal velocity gradient tensor (e.g., Wang and Shen, 2020):

$$\begin{aligned}
\dot{\varepsilon}_h &= \begin{bmatrix} \dot{\varepsilon}_{xx} & \dot{\varepsilon}_{xy} \\ \dot{\varepsilon}_{yx} & \dot{\varepsilon}_{yy} \end{bmatrix} = \begin{bmatrix} \frac{\partial V_E}{\partial x} & \frac{1}{2}\left(\frac{\partial V_E}{\partial y} + \frac{\partial V_N}{\partial x}\right) \\ \frac{1}{2}\left(\frac{\partial V_N}{\partial x} + \frac{\partial V_E}{\partial y}\right) & \frac{\partial V_N}{\partial y} \end{bmatrix} \\
\dot{\varepsilon}_{dil} &= \dot{\varepsilon}_{xx} + \dot{\varepsilon}_{yy} \\
\dot{\varepsilon}_{shear} &= \sqrt{\dot{\varepsilon}_{xy}^2 + (\dot{\varepsilon}_{xx} - \dot{\varepsilon}_{yy})^2/4} \\
\dot{\varepsilon}_{II_h} &= \sqrt{\dot{\varepsilon}_{xx}^2 + 2\dot{\varepsilon}_{xy}^2 + \dot{\varepsilon}_{yy}^2}
\end{aligned} \tag{11.15}$$

where V_E and V_N are the east and north velocities, and $\dot{\varepsilon}_{dil}$, $\dot{\varepsilon}_{shear}$ and $\dot{\varepsilon}_{II_h}$ are the dilatation, maximum shear, and second invariant of the horizontal strain rate tensor (Figure 11.4).

We can only obtain V_E in Equation 11.15 from InSAR by decomposing the LOS velocities from the ascending and descending tracks. For V_N, we rely on interpolating the GNSS north velocities (Figure 11.4(a)). Combining these two data sets is an art. Given the different spatial and noise characteristics of InSAR and GNSS as discussed in Section 11.1, there are several goals one might wish to achieve in this step: (1) Suppress noise while retaining the high resolution of the InSAR V_E; (2) Interpolate the irregularly spaced GNSS V_N without generating artifacts; (3) Settle on a resolution that allows InSAR to reveal tectonically interesting features without overstretching the GNSS resolution; otherwise, the V_N gradients can be significantly smoother than the V_E gradients, resulting in strain rate fields with unbalanced constituting components.

For applications where we expect the velocity field to be strictly increasing in one direction (e.g., deformation under a regional tectonic stress), median filtering the InSAR V_E is a powerful way to suppress noise, localize strain onto faults, and highlight creeping sections (Figure 11.4(b), Ou et al. (2022)). The appropriate filter window is a function of the velocity step and locking depth of the fault, as well as the noise level of the velocity field (Figure 11.5). Interpolating just the GNSS V_N can be achieved through fitting velocities using spatial basis functions such as splines (e.g., GMT surface) or employing geostatistical weighted neighborhood methods (e.g., kriging). The former requires assumptions that are not necessarily tectonic. The latter, if pushing the resolution too hard relative to the GNSS station spacing, can result in a ringing effect in the strain rate field at common radii to GNSS stations.

There are also two types of methods designed to work with both V_E and V_N, or even LOS velocities, at the same time. The first type is through inverting velocity vectors at vertices of either a fixed (*VELMAP*, Wang and Wright (2012)) or an ensemble of variable (Pagani et al., 2021) triangular mesh(es) and calculating

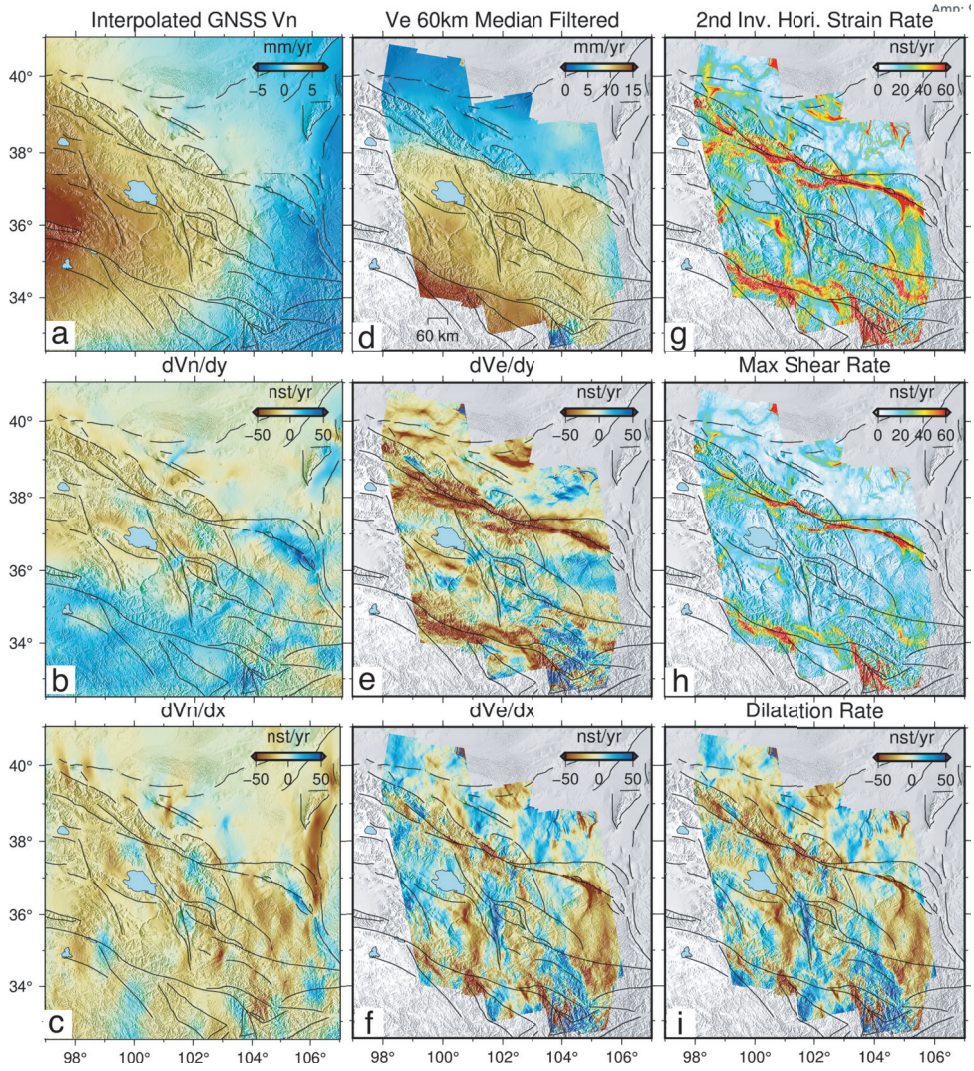

Figure 11.4 (a) Interpolated north velocities from GNSS. (b, c) Horizontal gradients of (a). (d) Median filtered InSAR east velocities. (e, f) Horizontal gradients of (d). (g) Second invariant of horizontal strain rate. (h) Maximum shear strain rate. (i) Dilatation rate (Ou et al., 2022).

strain rates within the mesh triangles. The second type is through velocity vector interpolation based on the physical assumption of elasticity (*gpsgridder*, Sandwell and Wessel (2016)) and the direct inversion of strain rates of stresses (Haines et al., 2015; Haines and Holt, 1993). For all, except the ensemble methods, the choice of the smoothing parameter has a strong influence on the resultant strain rate fields. The traditional L-curve method is a useful approach to balance model smoothness

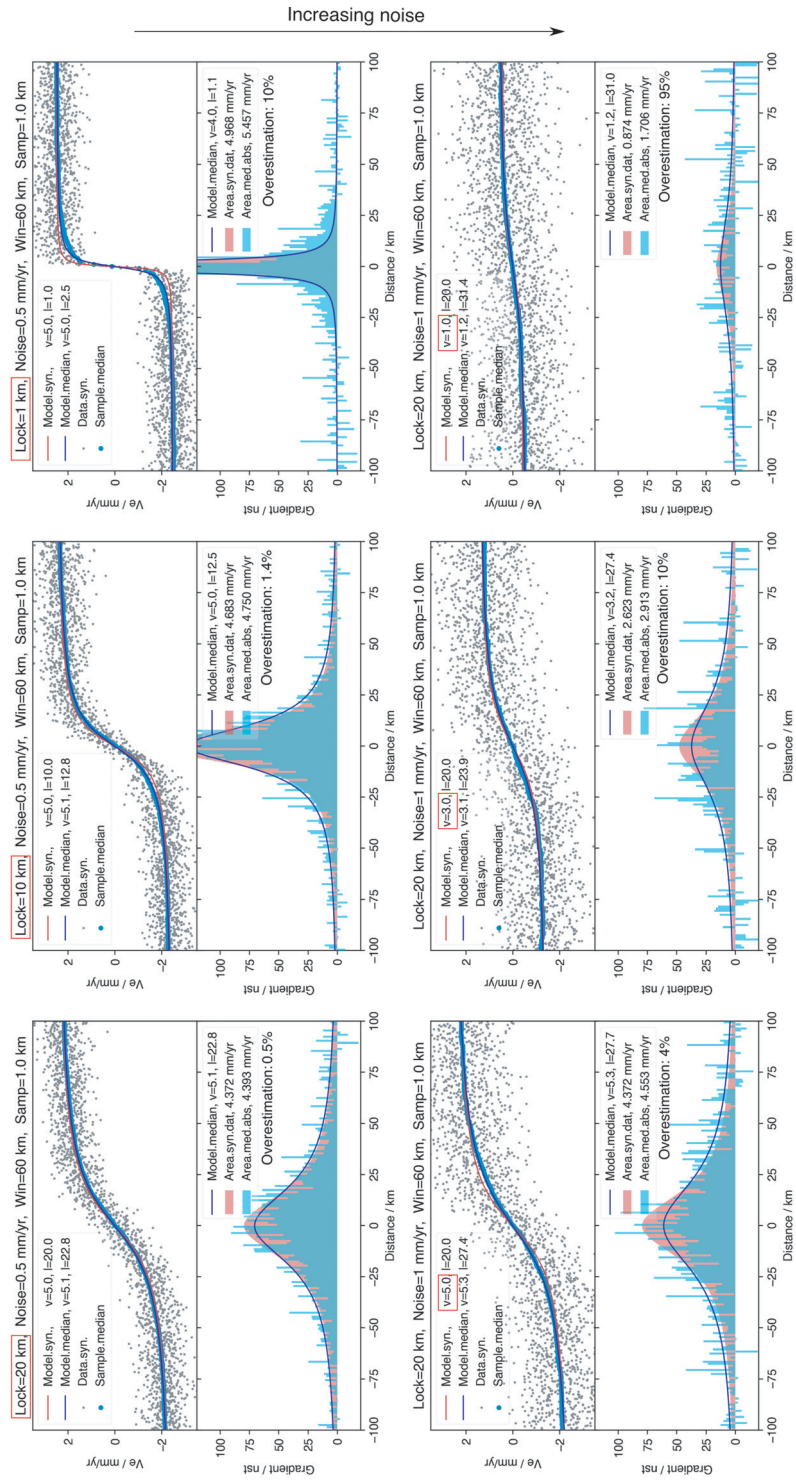

Figure 11.5 Synthetic tests of filtering a 1-D arctangent velocity profile (red line) with Gaussian noise (gray dots) with a median filter window of 60 km. A larger filter window is needed for smaller locking depths, higher noise, and smaller velocity steps across the fault (Ou et al., 2022).

and data misfit (Maurer and Materna, 2023) and is implemented in the open-source Python package, *Strain_2D* (Materna et al., 2021), which allows cross-comparison of strain rate fields from different methods.

11.5 InSAR/GNSS Time Series

InSAR and GNSS time series are useful for constraining deformation in different parts of an earthquake cycle (Liu et al., 2021; Guns et al., 2022), characterizing spatiotemporal variability of fault creep (Khoshmanesh et al., 2015; Li et al., 2023), detecting volcanic unrest (Gaddes et al., 2019; Liu et al., 2023), tracing groundwater recharge (Hu et al., 2021; Neely et al., 2021), and monitoring permafrost dynamics (Li et al., 2015; Daout et al., 2020a). The InSAR time series is generally more uncertain than the GNSS time series due to the lower temporal sampling rates (Figure 11.6). However, the spatial pattern of InSAR velocities coupled with

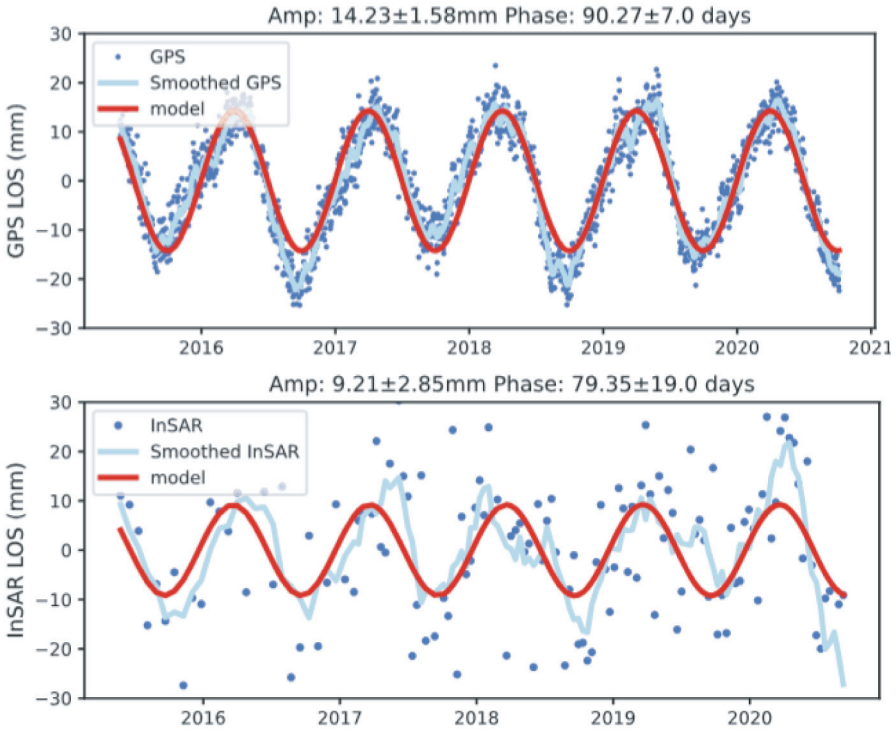

Figure 11.6 Comparison between continuous GNSS time series and InSAR time series extracted from a pixel colocated with GNSS station P242 in California (Li et al., 2023).

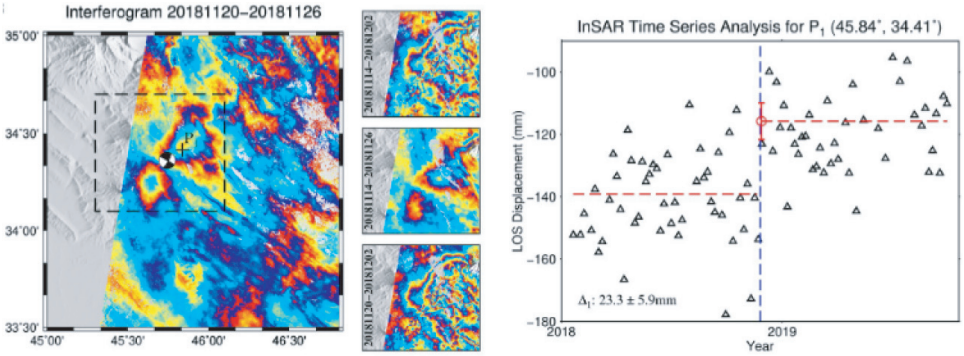

Figure 11.7 Four coseismic interferograms straddle the 2018 Nov 25 Mw 6.3 earthquake at the Iran–Iraq border. Fitting a step function to the noisy time series at pixel P_1 helps obtain a more accurate coseismic deformation field (Liu et al., 2021).

independent data sets often gives clues to the dominant deforming source in an otherwise blind mixture of latent deformation sources.

The knowledge of the temporal characteristics of the dominant deforming source is useful for deciding the linear combination of independent temporal components for parametric time series inversion. For small and deep earthquakes where surface deformation is small, fitting a Heaviside (step) function to the time series pixel by pixel can resolve a coseismic deformation field that is cleaner than the best single interferogram (Figure 11.7; Liu et al., 2021). For larger or shallower earthquakes where postseismic deformation is observable over months or years, fitting a logarithmic function following the Heaviside function helps resolve the coseismic and postseismic components of the earthquake cycle (Figure 11.8; Daout et al., 2019). Inverting cumulative creep on fault patches from InSAR time series can reveal spatial-temporal variations in creep kinematics (Figure 11.9; Khoshmanesh et al., 2015). Surface deformation induced by groundwater withdrawal and recharge often exhibits seasonal oscillations. The amplitude and phase of the sinusoidal functions are indicative of groundwater level fluctuations and flow timing and paths (Figure 11.10; Neely et al., 2021). Similar sinusoidal patterns can be observed on high mountains experiencing permafrost freeze-and-thaw cycles (Daout et al., 2020a). Net subsidence rate suggests overall decay of mountain permafrost due to climate change, and the increasing amplitude of the seasonal oscillation suggests increasing permafrost active layer thaw (Figure 11.11).

When the purpose is to detect changes such as the onset of volcanic unrest, independent component analysis is an effective tool (Ebmeier, 2016; Gaddes et al., 2018). This method is particularly useful for automatically monitoring global active volcanoes. Independent component analysis is performed on the historical time

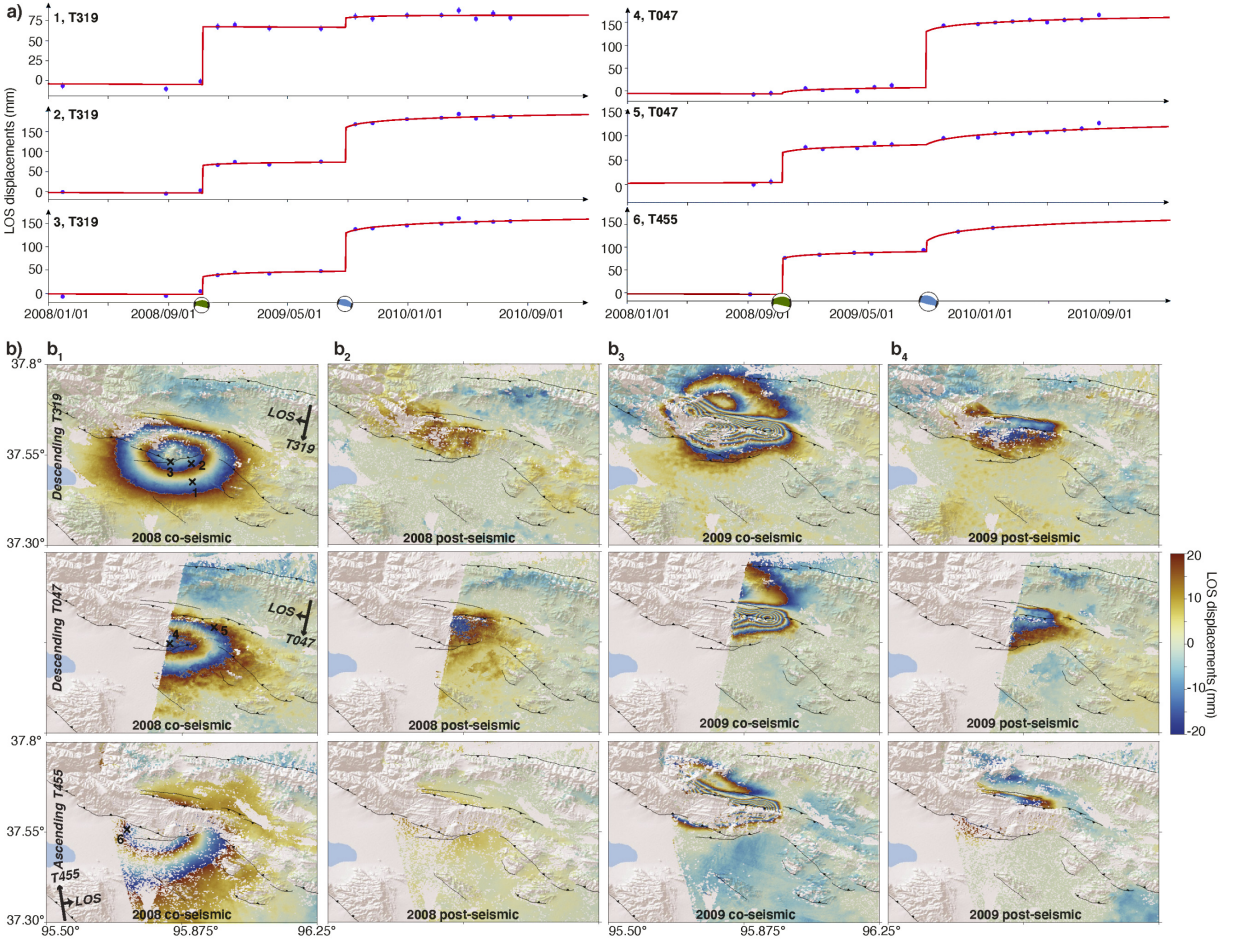

Figure 11.8 Two Heaviside functions followed by logarithmic decays fitted to time series to extract coseismic and postseismic deformations of an earthquake doublet in the Qaidam basin in 2008 and 2009 (Daout et al., 2020b).

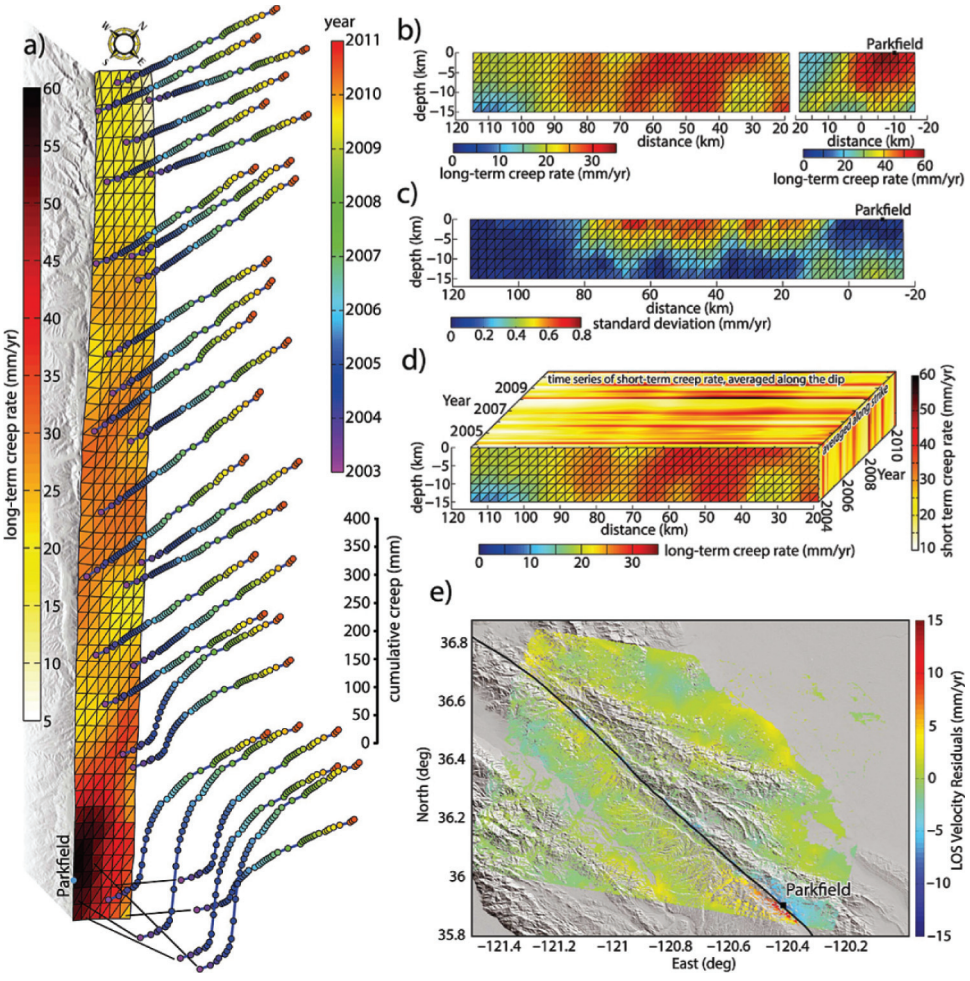

Figure 11.9 Inverted spatial-temporal variation of creep along the Central Segment on the San Andreas Fault (Khoshmanesh et al., 2015).

series to obtain a set of spatially independent sources, which are used to fit the future interferograms. An unrest is flagged when either the relative importance of the independent components changes or the misfit changes significantly (*LiCSAlert*; Figure 11.12; Gaddes et al. (2019)).

It is also possible to infer large-scale deformation sources by investigating temporal characteristics of the time series. Lemrabet et al. (2023) analyzed the time series of range and azimuth coefficients of planar ramps inverted from InSAR time series (Maubant et al., 2020) to identify dominant periodicity in the large-scale features (Figure 11.13). The fortnightly periodicity in the atmospheric delay-corrected time series represents solid earth tide.

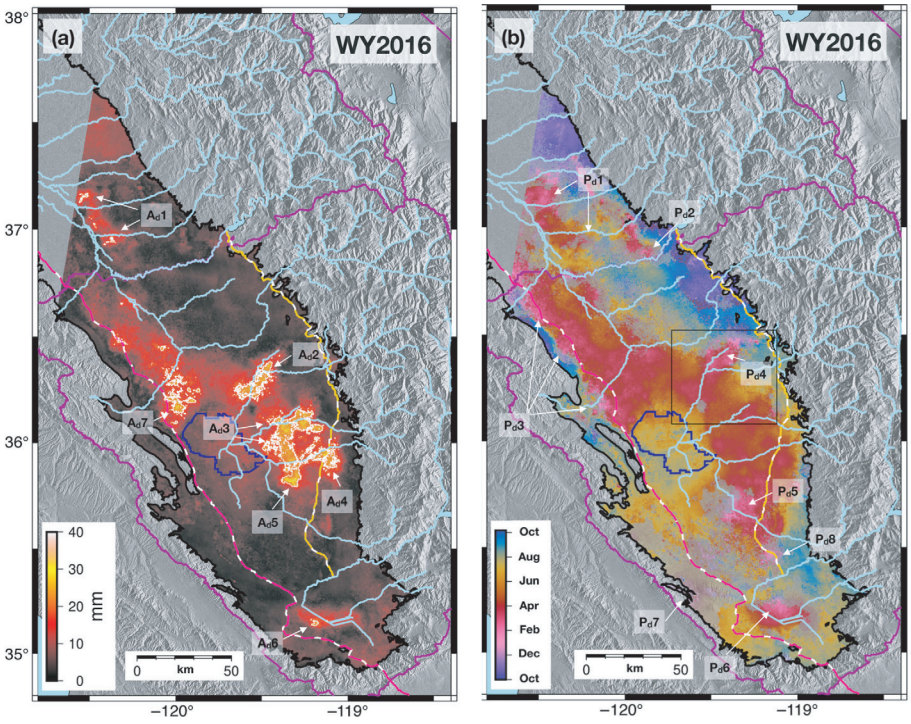

Figure 11.10 Seasonal (a) amplitude and (b) phase of LOS displacement during the water year 2016 in California's San Joaquin Valley (Neely et al., 2021).

11.6 Problems

1. How would you correct the long-wavelength errors in InSAR displacement and velocity mapping in the following cases: (1) dense GNSS stations available with continuous time series; (2) dense GNSS stations available with data available only as long-term averaged velocities and not time series; (3) sparse GNSS stations relative to SAR swath width; (4) no GNSS data available.
2. Generalize Equation 11.11 for cases where the pixel is not exactly in the center range of the ascending and descending SAR images. Derive the (e, n, u) unit look vectors from an arbitrary ground pixel $\mathbf{x}_o$ to the satellites in the ascending and descending orbits at positions $\mathbf{x}_s^a$ and $\mathbf{x}_s^d$, respectively (Figure 11.2). This equation is rank-deficient. How would you approach solving this equation?
3. Why is a larger filter window needed for median filtering the arctangent-shaped velocity profile with smaller locking depths, higher noise, and smaller velocity steps across the active fault for strain rate calculations (Figure 11.5)?
4. How would you construct the linear equations for parametric time series inversion? Consider a time series affected by an earthquake happening at time t_e

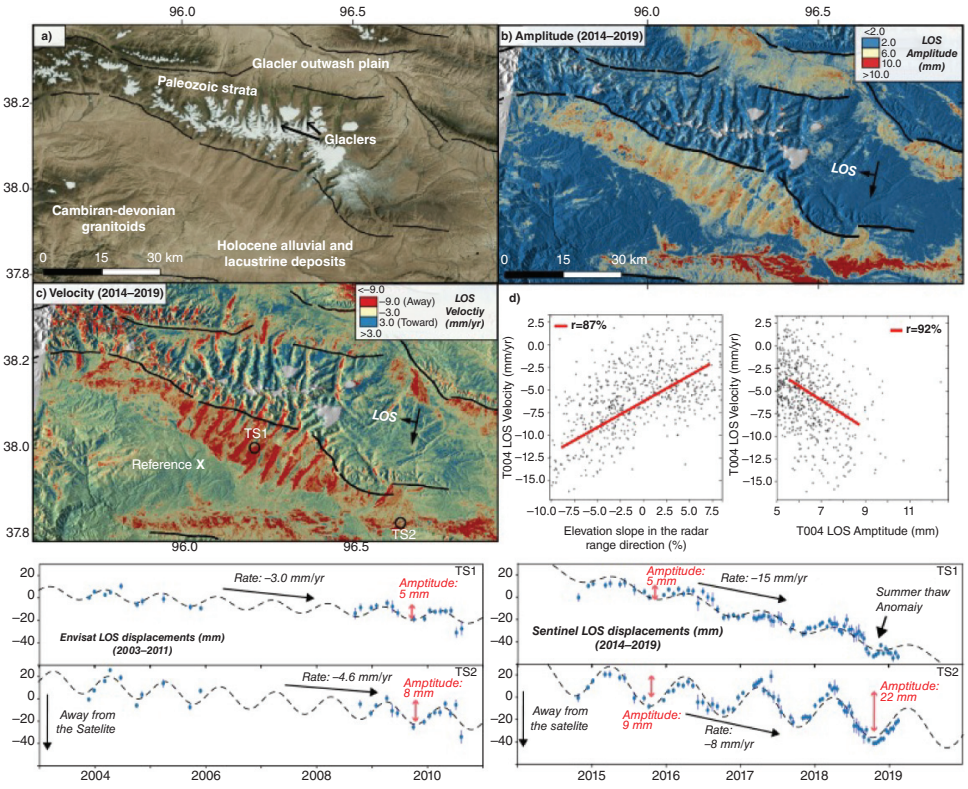

Figure 11.11 (a) Satellite imagery, (b) seasonal amplitude, and (c) LOS velocity over western Qilianshan. (d) Correlation between LOS velocity and topographic gradient. (e) Time series showing increasing amplitude of seasonal oscillations over time (Daout et al., 2020a).

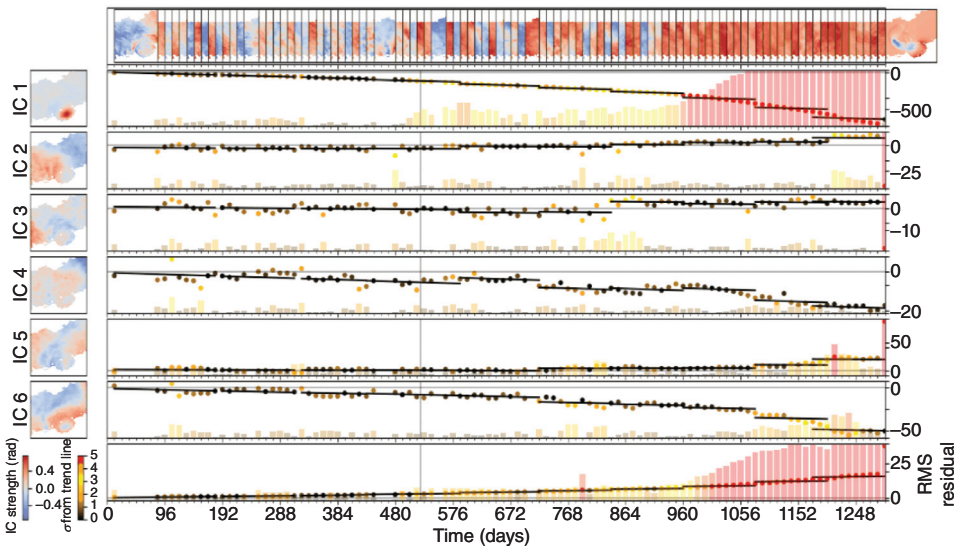

Figure 11.12 Detecting volcanic unrest using significant changes in the relative weighting of different independent components and the ability to fit the time series with independent components, implemented in *LiCSAlert* (Gaddes et al., 2019).

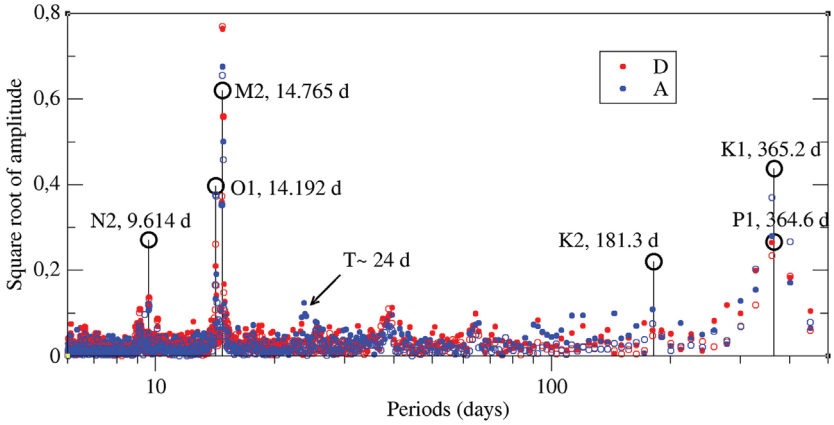

Figure 11.13 Lamb-Scargle periodogram for observed (filled circles) and modeled (open circles, alias periods for Sentinel-1, 6-day repeat, Table 9.2) solid Earth tide time series in range inverted from descending (red) and ascending (blue) tracks (Lemrabet et al., 2023).

followed by postseismic deformation with a logarithmic decay with characteristic time τ, in an area experiencing permafrost decay due to global warming with seasonal freeze-and-thaw cycles of increasing seasonal amplitude over time (Figures 11.8 and 11.11).